Carbon 246 (2026) 120926

Contents lists available at ScienceDirect

Carbon

journal homepage: www.elsevier.com/locate/carbon

Interfacial engineering of boron carbonitride via tuning layers for enhanced solar water oxidation

Lin Wu [a], Svetlana V. Belaya [b,*], Lixiang Li [a], Eugene A. Maksimovskiy [b], Alexei N. Kolodin [b], Igor P. Asanov [b], Alexandr G. Plekhanov [b], Ilya V. Korolkov [b], Han Zhang [a], Marina L. Kosinova [b,**], Baigang An [a,***]

[a] Key Laboratory of Energy Materials and Electrochemistry Research Liaoning Province, School of Chemical Engineering, University of Science and Technology Liaoning, Anshan, 114051, China
[b] Nikolaev Institute of Inorganic Chemistry SB RAS, Novosibirsk, 630090, Russia

ARTICLE INFO

Keywords:
One-stop approach
Boron carbonitride nanowalls
Tuning layer
Photoelectrochemical water oxidation

ABSTRACT

Metal-free boron carbonitride (BCN) has attracted considerable interest for photoelectrochemical water splitting applications. However, its utility is limited by inadequate charge carrier transport, serious charge recombination and suboptimal surface catalytic activity. Herein, we propose a novel boron carbon (BC_x) tuning layer strategy to address these limitations. By employing an integrated one-stop approach, BCN nanowalls are vertically grown on BC_x film surfaces via plasma-enhanced chemical vapor deposition (PECVD) for fabrication photoelectrodes. Experimental analyses and band structure studies confirm that the BC_x tuning layer not only promotes the formation of vertically aligned BCN nanowall arrays, but also serves as an efficient electron transfer pathway for photogenerated electrons. This inhibits charge recombination and enhances charge separation, thereby making more holes available as active sites for photoelectrochemical reactions. Consequently, the BCN/BC_x photoanode achieves a water oxidation photocurrent of 0.82 mA cm^{-2} at 1.23 V, a 4.6 times improvement over pristine BCN. Furthermore, the BCN/BC_x photoanode demonstrates remarkable stability, maintaining a steady photocurrent under continuous illumination for 100 h. This innovative tuning layer strategy offers promising prospects for advanced applications in catalysis, sensors, transistors and beyond.

1. Introduction

Solar energy conversion is widely regarded as one of the most promising strategies to address the global energy crisis caused by the depletion of fossil fuels [1–3]. Among various approaches, photoelectrochemical (PEC) water splitting has attracted significant attention for its ability to directly convert solar energy into chemical energy [4,5]. Metal-free photocatalysts are composed of low-cost, earth-abundant elements, including carbon, nitrogen, oxygen and boron. These lightweight, corrosion-resistant elements can be strategically engineered into durable compounds with tunable photophysical characteristics, rendering them highly promising for applications in photocatalysis and solar energy conversion. Notable examples include graphitic carbon nitride (g-C_3N_4) [6,7]. boron phosphide (BP) [8] and boron carbonitride (BCN) [9], as well as the boron carbide [10]. Among these photoanode candidates, BCN stands out as a leading candidate for efficient PEC water splitting, owing to its tunable band gap [11,12] and energy levels well-aligned with the water redox potentials [12–14]. However, the sluggish kinetics of BCN and high charge recombination leads to a gap between the photocurrent density and the theoretical expectation [15]. In recent decades, significant attention has been given to development of BCN photoanodes with high photocurrent densities, sufficient anodic onset potentials and high fill factors through strategies such as elemental doping [16,17]. heterojunction construction [18,19] and introduction cocatalysts [20]. For instance, by optimizing the fluorine-doping BCN ratios, studies have demonstrated optimized band structures and enhanced electron transfer, further showcasing BCN's potential in advanced catalytic systems [21]. Ahsan et al. developed 0D-2D BCN

* Corresponding author.
** Corresponding author.
*** Corresponding author.
E-mail addresses: sveta@niic.nsc.ru (S.V. Belaya), marina@niic.nsc.ru (M.L. Kosinova), bgan@ustl.edu.cn (B. An).

https://doi.org/10.1016/j.carbon.2025.120926
Received 21 July 2025; Received in revised form 12 September 2025; Accepted 8 October 2025
Available online 10 October 2025

nanosheets integrated with C_{60} heterostructures [22], which exhibited multifunctional electrocatalytic capabilities for the hydrogen evolution reaction (HER), oxygen evolution reaction (OER) and oxygen reduction reaction (ORR).

Recently, electron transport layer has played a crucial role in facilitating efficient charge transport and suppressing charge recombination. While strategies such as doping, heterojunction construction, and cocatalyst introduction have been widely investigated to improve PEC activity, the incorporation of this layer presents a unique solution to the challenges of charge transport and separation. The significance of the electron transport layer in PEC systems cannot be overstated, as it has demonstrated exceptional effectiveness in devices like organic light-emitting diodes and perovskite solar cells by improving carrier mobility and device stability [23,24]. Leveraging these advancements in PEC systems could pave the way for achieving higher solar-to-chemical conversion efficiencies. The potential to enhance the light-harvesting capability and carrier transport efficiency of BCN in PEC catalysis via the introduction of an electron transport layer strategy remains largely unexplored. Currently, various methods are used to obtain BCN catalysts, such as high temperature polymerization, template synthesis, and hydro/solvo-thermal synthesis, which require high temperatures and complex reagent mixtures [25,26]. These processes often introduce impurities, wrinkles, or fractures in the BCN film, compromising its structural integrity. Such defects not only disrupt the van der Waals dielectric surface but also lead to interfacial voids or poor electrical contact, thereby diminishing the overall catalytic performance [27,28]. Thus, there is an urgent need to develop a low-temperature, integrated and highly efficient photocatalytic BCN electrode strategy incorporating an electron transport layer.

Herein, we report a one-stop approach for photoelectrodes fabrication, in which BCN/BC_x/FTO/glass structures are synthesized by first growing BC_x via low-pressure chemical vapor deposition (LPCVD), followed by the growth of BCN through plasma-enhanced chemical vapor deposition (PECVD). The BC_x layer functions as a tuning layer to regulate the charge recombination of boron carbonitride (BCN) nanowall arrays, thereby enhancing the utilization efficiency of photogenerated carriers. The synthesized BC_x layer, possessing a low conduction band, can concurrently enhance the charge carrier transport efficiency, prolonged lifetime of the excited state and surface water oxidation kinetics of BCN. The optimized microstructure and compositional synergy significantly enhance the PEC photocurrent density and charge carrier separation efficiency. The photoelectrochemical water oxidation reaction based on the BCN/BC_x photoanode is successfully achieves with a high photocurrent density of 0.82 mA cm^{-2} at 1.23 V, which is 4.6 times higher than that of pristine BCN, with a higher carrier concentration (1.19×10^{21} cm^{-3}) along with exhibit excellent stability for over 100 h. This strategy provides new insights into the introduction of tuning layer in PEC water oxidation systems.

2. Experimental section

2.1. One-stop approach synthesis of a photoelectrode

BCN/BC_x/FTO/glass structures were synthesized in a quartz tube reactor by chemical vapor deposition method. Low-pressure chemical vapor deposition (LPCVD) and plasma-enhanced chemical vapor deposition (PECVD) were used for BC_x and BCN layers formation, respectively. The synthesis setup is shown in Scheme 1. Trimethylamine borane vapor (TMAB, $(CH_3)_3N{\cdot}BH_3$) (97 % pure, Sigma-Aldrich, Merck Ltd., Germany) and nitrogen (ultrahigh purity grade, Russia) were mixed as precursors for the synthesis of both layers. Fluorine-doped tin oxide (FTO) with average resistivity of 7 Ω/□ coated on glass slides were used as the substrates (1×2 cm^2 size) for photoanode formation. Semiconducting n-type Si(100) wafers (KEF-4.5) of the dimensions of $10 \times 10 \times 0.47$ mm^3 were used as substrates for investigation of films by FTIR spectroscopy, X-ray photoelectron spectroscopy (XPS), atomic force microscopy (AFM), scanning electron microscopy (SEM), and ellipsometry. Both LPCVD and PECVD depositions were performed at a temperature of 673 K. For the PECVD process, a radiofrequency (27.12 MHz) plasma was employed at a power of 20 W. The partial pressures of TMAB and nitrogen were maintained at 9×10^{-3} Torr and 3×10^{-3} Torr, respectively. The BC_x layer was deposited for 5 min, 15 min and 30

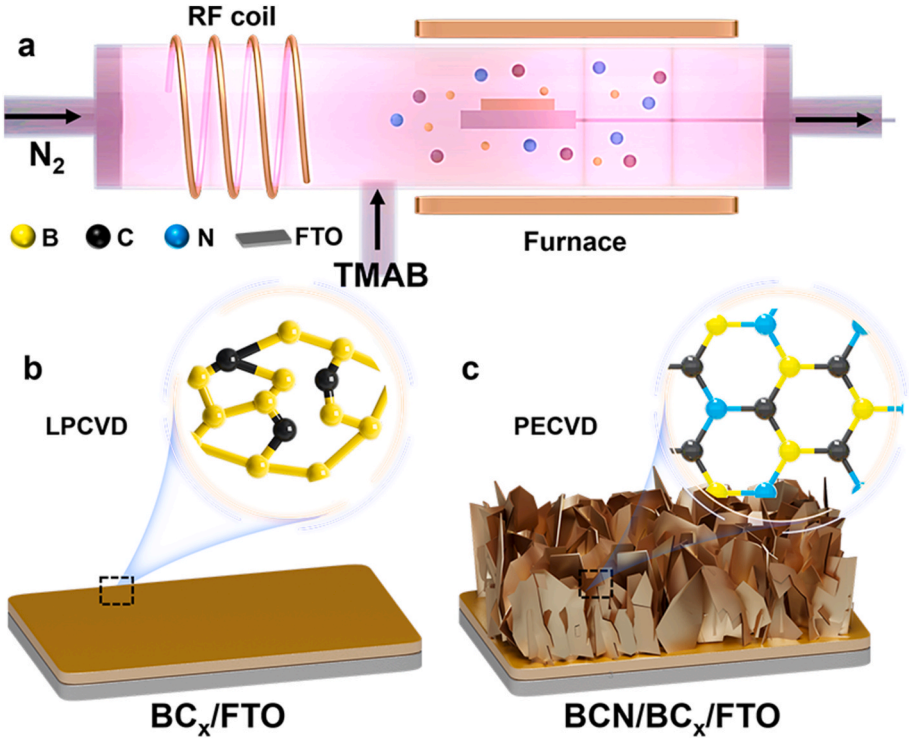

Scheme 1. Schematic diagram of one-stop synthesis of BCN/BC_x photoanodes on FTO/glass substrate.

min to control its thickness. The growth of BCN nanosheets on the BC_x layer surface continued for 60 min using PECVD. The titles and parameters of the films synthesized are listed in Table S1.

2.2. Structure characterization

The morphology of the film surface was investigated using scanning electron microscopy JSM-6700F (JEOL, Japan), with a Quantax 200 (Bruker, Germany) EDX attachment at 3 keV. Transmission electron microscopy (TEM) observations were carried out using a Hitachi H-800 TEM (Hitachi, Japan) operated at an accelerating voltage of 200 kV. Topography of a samples was investigated using a Ntegra Prima II atomic force microscope (AFM) (NT-MDT, Russia) in semi-contact mode. An HA_NC (A) cantilever was used, with the following parameters: cantilever length 123 μm, width 34 μm, thickness 3 μm, radius of curvature 10 nm, force constant 17 N/m and resonance frequency 230 kHz. Root mean square (RMS) surface roughness was calculated according to the ISO 4287-1 standard using Nova SPM software. X-ray diffractometry measurements were performed on a D8 Advance powder diffractometer (Bruker, Germany) using Cu Kα radiation (linear LYNXEYE XE-T detector) at a grazing angle of 0.5° in 2θ-scanning mode. Diffraction patterns of the samples were obtained in the range of angles $2\theta = 20°–50°$ with a step of 0.03° and 60 s per step. UV–Vis diffuse reflectance spectra in the solid state were measured with a Shimadzu U-3000 spectrophotometer (Shimadzu, Japan). Raman spectra were performed using a LabRAM HR Evolution Raman (Horiba, Japan) with a 532 nm laser as excitation source. Chemical structure of films was studied using FTIR absorption spectra recorded on a SCIMITAR FTS 2000 spectrometer (Digilab, USA) in the wavenumber range of 375–4000 cm^{-1} with a resolution of 2 cm^{-1}. Photoluminescence (PL) spectra were obtained with an Edinburgh LP 980 spectrophotometer. X-ray photoelectron spectroscopy (XPS) were performed on a FLEXPS system (Specs, Germany). Spectral excitation was provided by a monochromatic Al Kα source, with analyzer operated at a pass energy of 20 eV. The chamber pressure was maintained at ~7.5×10^{-11} Torr during analysis.

2.3. Photoelectrochemical measurements

PEC measurements were conducted using a CHI750E electrochemical workstation (CH Instruments Inc., Shanghai, China) in a standard three-electrode configuration. Pt wire served as counter electrode and a Hg/HgO electrode was employed as the reference. All experiments were carried out in 1 M KOH aqueous electrolyte under alkaline conditions. The electrolyte solution was vigorously stirred and bubbled with N_2 for 0.5 h to ensure that O_2 in the PEC cell was completely removed. Illumination was provided by a 150 W Xe lamp, delivering a light intensity of 100 mW cm^{-2} onto photoanode surface. After depositing BC_x, BCN and BCN/BC_x layers, copper tape was affixed to exposed edges of the substrate glass for electrical contact. All electrodes were housed in a quartz electrochemical cell. Photocurrent responses were recorded via linear sweep voltammetry at a scan rate of 5 mV s^{-1}. Applied bias photon-to-current efficiency (ABPE) was calculated according to the following equation:

$$ABPE = J \times (1.23 - E_{RHE}) / P_{light} \quad (1)$$

Here, E_{RHE} represents bias *vs.* reversible hydrogen electrode (RHE); J denotes photocurrent density at the corresponding bias and P_{light} refers to illumination intensity, set at 100 mW cm^{-2}. E_{RHE} was calculated by:

$$E_{RHE} = E_{Hg/HgO} + 0.098 + 0.059 \times pH \quad (2)$$

where $E_{Hg/HgO}$ represents bias *vs.* RHE (as used in this work), while the standard electrode potential of *Hg/HgO* reference electrode is denoted by $E_{Hg/HgO}$.

Charge separation efficiency (η_{sep}) and charge injection efficiency (η_{trans}) were calculated by using 0.5 M Na_2SO_3 solution electrolyte as hole scavenger.

$$\eta_{sep} = \frac{J_{Na2SO3}}{J_{abs}} \times 100\% \quad (3)$$

$$\eta_{trans} = \frac{J}{J_{abs}} \times 100\% \quad (4)$$

where J, J_{Na2SO3} and J_{abs} are photocurrent density in KOH, photocurrent density in NaOH with Na_2SO_3 and photon absorption rate expressed as current density, respectively. Electrochemical impedance spectroscopy (EIS) was performed under illumination by applying a 5 mV AC perturbation at 0.67 V vs. Hg/HgO, across a frequency range spanning from 100 kHz to 0.01 Hz. Mott-Schottky analysis was conducted at a fixed frequency of 1 kHz with DC bias swept from −0.7 V to 0.5 V. The electrochemical surface area (ECSA) was calculated from the electric double-layer capacitance (C_{dl}) measured in a potential window without Faradaic response. Cyclic voltammetry (CV) curves were recorded at scanning rates of 10–60 mV s^{-1} within the potential range of 1.03–1.13 V vs. RHE. Oxygen evolution under photoelectrochemical conditions was quantified using a custom-designed, airtight, transparent electrochemical cell.

$$N_d = \frac{2}{e\varepsilon\varepsilon_0}\left(\frac{d\left(\frac{1}{c^2}\right)}{dV_s}\right)^{-1} \quad (5)$$

where V_s is the applied potential, ε_0 is the vacuum permittivity (8.86×10^{-14} F m^{-1}), ε is the dielectric constant of semiconductor (4 for BCN), e is the electronic charge (1.6×10^{-19} C) [29], N_d is the carrier concentration.

$$\tau_{avg} = \frac{A_1\tau_1^2 + A_2\tau_2^2}{A_1\tau_1 + A_2\tau_2} \times 100\% \quad (6)$$

where τ_{avg} is the average lifetime, A_i is the pre-exponential factor and τ_i is the decay time.

3. Results and discussion

3.1. Material structure and characterization

The one-stop BCN/BC_x/FTO photoanode synthesis process is illustrated in Scheme 1. The growth of BCN nanowalls is highly dependent on the partial pressure ratio of trimethylamine borane (TMAB) to N_2 in initial gas mixture. To synthesize two-layer structure of photocatalyst, the first layer was formed by low-pressure chemical vapor deposition (LPCVD) of the initial gas mixture. When synthesizing the second layer, a plasma-enhanced chemical vapor deposition (PECVD) process was used. In these two processes, the substrate temperature and the reagent ratio were constant (Fig. S1). By adjusting the LPCVD process duration from 5 to 30 min, the thickness of the BC_x layer was controlled within the range of 10 ± 5 to 43 ± 5 nm, as determined by ellipsometry (Fig. S2). This demonstrates precise tunability of the BC_x layer thickness. Since the synthesis time of BCN layer was 60 min for all samples, its thickness in the structures was in the range of 273 ± 10 nm according to SEM data (Fig. S3). As depicted in the inset of Fig. 1d, digital images of samples exhibit a consistent coloration across the surface, suggesting excellent film uniformity.

The morphology of the BCN/BC_x films was examined using scanning electron microscopy (SEM). Fig. 1a shows BC_x layer is a highly uniform thin film. Fig. 1b–d presents top-view and cross-sectional images of BCN/BC_x films, demonstrating that BCN layers are highly uniform two-dimensional vertical nanosheets. EDX analysis of the BC_x layer shows a boron content of ~70 at.% and a carbon content of ~30 at.%. Consistent with literature data, BC_x is synthesized during LPCVD process [30].

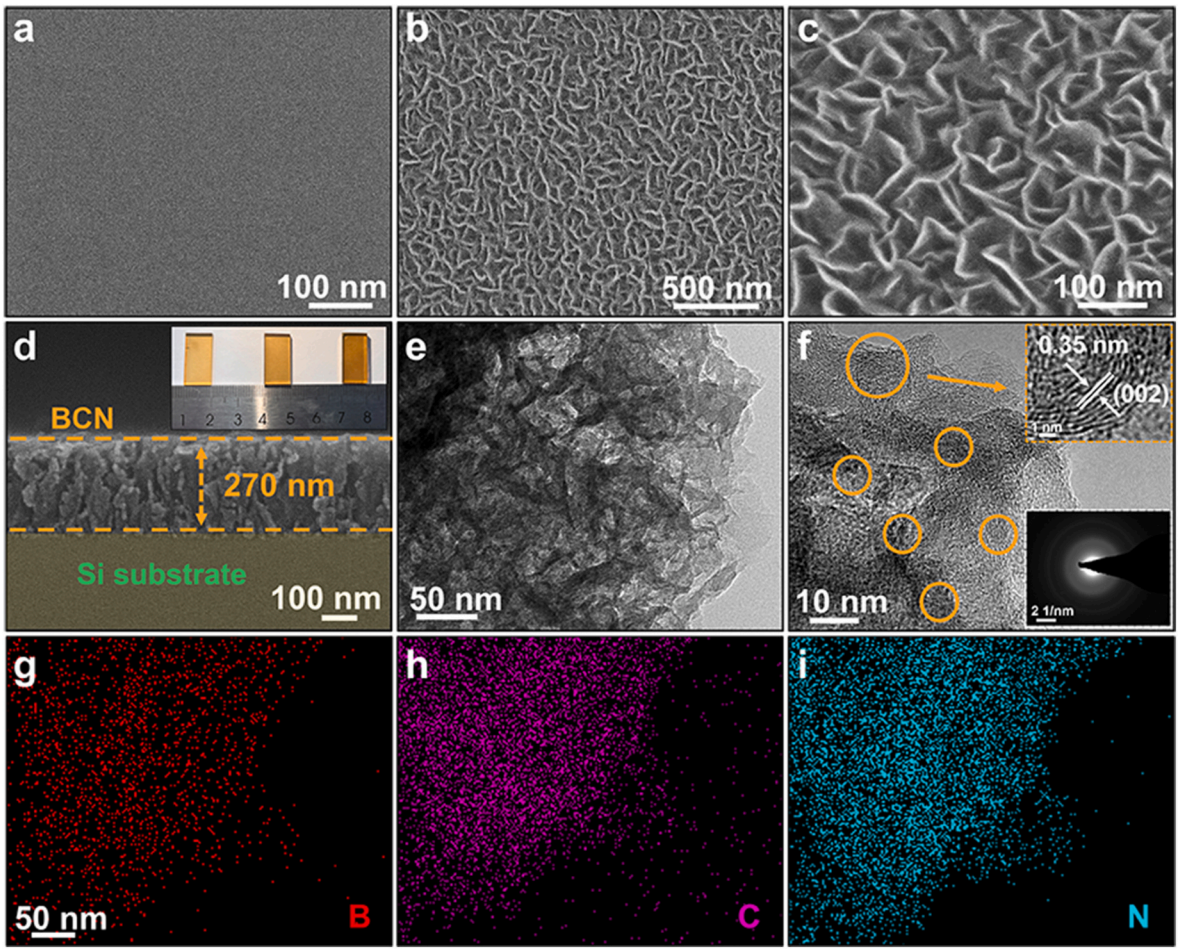

Fig. 1. (a) The top-view SEM image of the BC_x photoanodes layer. (b, c) The top-view and (d) cross-sectional view SEM images of the BCN/BC_x photoanodes films (BCN/BC_x-15 sample); the inset of (d) presents photographs of BCN/BC_x-X/FTO/glass samples. (e) TEM image of the BCN/BC_x film. (f) HR-TEM image of BCN/BC_x-15 film; the inset shows the HR-TEM images and selected area electron diffraction (SAED) pattern. (g–i) TEM-EDS element mapping of B, C and N elemental.

Transmission electron microscopy (TEM) of the typical BCN/BC_x sample revealed a nanosheet structure as shown in Fig. 1e. Selected-area electron diffraction (SAED) patterns suggest polycrystallinity of the BCN, indicating that carbon forms domains (inset of Fig. 1f) [31]. High-resolution TEM (HR-TEM) images (Fig. 1f) reveal well-ordered graphite-like layers with a precise lattice spacing of 0.35 nm [32,33] (Fig. 1f and inset). The chemical composition was further analyzed via scanning transmission electron microscopy (STEM) coupled with energy-dispersive X-ray (EDX) analysis, which provided elemental mappings of B, C, and N, showing a uniform distribution of the three elements within the BCN film (Fig. 1g–i and Fig. S4).

Fig. 2a–c presents the atomic force microscopy (AFM) images and Table S1 provides data on the root-mean-square (RMS) roughness of the BC_x, BCN and BCN/BC_x layer surface. The RMS roughness of BC_x layers was investigated as a function of deposition time. As shown in Fig. S5, the RMS roughness varied between 0.2 and 0.3 nm as the deposition time increased from 5 to 30 min. The RMS roughness of the BCN nanosheets synthesized directly via PECVD is 2.6 nm. When the BCN/BC_x film is synthesized using one-stop approach, the RMS roughness ranges in the interval of 1.9–2.5 nm (Fig. 2c and S6). These changes in RMS roughness highlight that the morphology of BCN nanosheet growth is significantly influenced by the underlying BC_x layer. As shown in Fig. S7, the low RMS roughness indicates the uniformity of the height of the vertically aligned BCN nanowalls [34], a crucial morphological characteristic for photoelectrochemical applications. This structural precision ensures that the sub-wavelength dimensions of the nanowalls effectively minimize optical scattering losses. Additionally, the nanomaterials' high specific surface area aids charge transfer via contact surfaces, lessening the current density and overvoltage of oxidation-reduction reactions. Thus, the strong light-harvesting capability of vertically aligned BCN nanowalls is crucial for achieving efficient PEC water splitting performance.

Further characterization of the nanofilm composition was conducted using Fourier transform infrared (FTIR) Spectroscopy (Fig. 2d and S8) and Raman spectroscopy (Fig. S9). As reported in previous studies, the FTIR spectrum of crystalline, carbon-free hexagonal boron nitride (h-BN) displays two distinct absorption bands: one corresponding to in-plane B–N stretching vibrations ($\nu||$ = 1370-1400 cm^{-1}), which are primarily influenced by distortions within the basal planes and another associated with out-of-plane B–N–B bending modes ($\nu\perp$ = 790-817 cm^{-1}), whose spectral features are governed by the stacking arrangement of the layers [35]. Turbostratic boron nitride (t-BN), a hexagonal graphite-like form characterized by a disordered structure lacking long-range order and exhibiting an expanded interlayer spacing, shows the same two characteristic FTIR bands as crystalline h-BN; however, these bands appear broader and exhibit noticeable shifts [36]. The presence of carbon in the h-BN structure affects the position of these two absorption peaks. Out-of-plane vibrations are shifted to lower wave numbers [37]. In the FTIR spectra of BCN films (Fig. 2d and S8), peaks at 1382–1388 cm^{-1} and 809–810 cm^{-1} correspond to in-plane B–N stretching and out-of-plane N–B–N bending vibrations, respectively, indicating the sp^2-hybridized structure of turbostratic BN, while there are no corresponding vibration in BC_x [37]. There is a shoulder at 1570 cm^{-1}, which can be attributed to vibrations of the C═C/C═N bonds. In

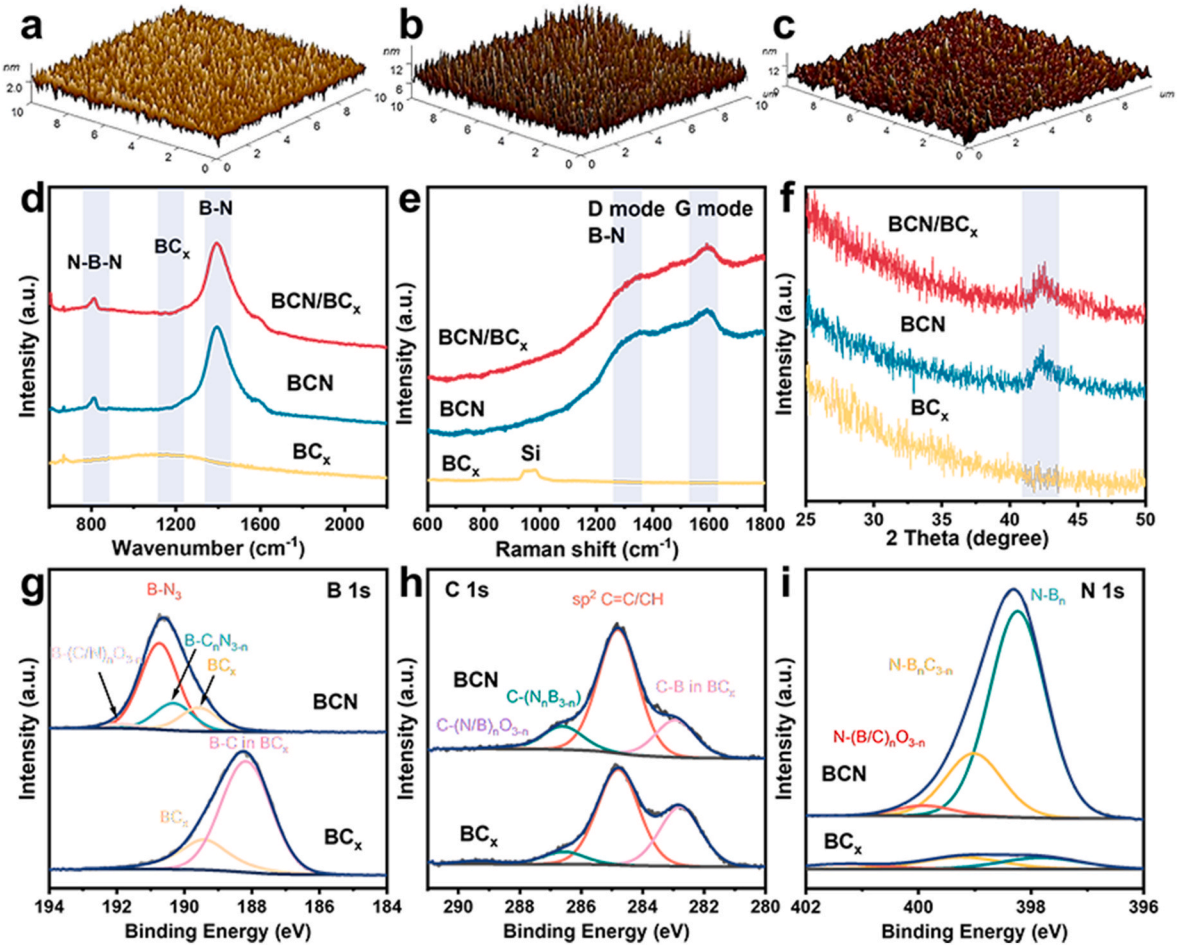

Fig. 2. (a–c) 3D AFM images of the BC_x, BCN and BCN/BC_x surfaces, respectively. Scanning area is 10 × 10 μm^2. (d–f) FTIR. Raman spectra and XRD patterns of the BCN/BC_x, BCN and BC_x samples. XPS high-resolution spectra of (g) B 1s, (h) C 1s and (i) N 1s of BCN and BC_x.

the FTIR spectra of BCN/BC_x/Si(100) structures, there is a very week band at 1100 cm^{-1} which corresponds to a-BC_x layer.

Raman spectrum of the amorphous or disordered carbon shows two broad peaks centered at approximately 1350 cm^{-1} (D mode) and 1580 cm^{-1} (G mode) [38]. Boron nitride in Raman spectrum has a characteristic band around 1370 cm^{-1} corresponding to the E_{2g} mode of the hexagonal BN phase [35]. Fig. 2e and S9 present the Raman spectra of BC_x, BCN nanofilm and BCN/BC_x layers. The BC_x thin film spectrum has no peculiarities in the region of 800–1800 cm^{-1}. Raman spectra of BCN and BCN/BC_x films have a broad band with two peaks centered at approximately 1360 and 1590 cm^{-1}. Exact nature of 1360 cm^{-1} peak is not determinable due to the overlap of BN E_{2g} mode and carbon D mode in this region. But we can assume that the BN peak does take place, since according to the abovementioned FTIR spectra and XPS data presented below, where B–N bonds are observed. The Raman spectra's carbon features, along with the C═C and/or C═N bonds identified in FTIR spectra, confirm inclusion of graphene domains within the h-BN lattice. Furthermore, BCN and BCN/BC_x XRD patterns exhibit one broadened reflection at $2\theta = 42.4°$ (Fig. 2f), which corresponds to diffraction on a family of (100) planes in h-BN [39]. TEM analysis revealed interlayer spacings of 0.35 nm [17,40]. The XRD pattern of BC_x film demonstrates an amorphous state of the layer.

The surface chemical state, bonding structure, and elemental composition of BC_x layer and the BCN nanowalls were further analyzed by XPS. The survey spectra of both films revealed the presence of elemental signals corresponding to B, C, N, and O. The compositions are $B_{0.70}C_{0.21}N_{0.04}O_{0.05}$ and $B_{0.38}C_{0.26}N_{0.32}O_{0.04}$ for BC_x film and BCN film, respectively. More detailed information on the chemical structure of the samples were provided by high-resolution XPS spectra for B 1s, C 1s and N 1s (Fig. 2g–i). The spectra reveal asymmetric and broadened peaks, indicating the presence of multiple bonding configurations for the atoms. For BC_x sample synthesized via LPCVD, the core level spectrum of B 1s is composed of three components (Fig. 2g, bottom). The dominant component at 188.2 eV corresponds to B–C bonds in "boron-rich" in boron carbide (BC_x) [41,42]. Components with lower intensity at189.4 can be attributed to boron atoms bonded to carbon in the B–C bonds [43,44]. Fig. 2h presents the C 1s spectrum, which displays complex fine structure. Main component at 284.8 eV corresponds to sp^2-bonded carbon atoms and hydrocarbons. The intensive peaks at 282.8 can be subscribed to C–B bonds in BC_x. The peaks at 286.6 is attributed to C–N bonds in C-$(N/B)_n$ hybrid bonds and a weak peak at 289.3 eV is considered as carboxyl group on a film surface. Deconvolution of the N 1s peak of BC_x film spectrum identifies main components: N-B_nC_{3-n} bonds and N-$(B/C)_nO_{3-n}$ bonds in h-BC_xN_y at 398.6 and 401.4 eV, respectively. O 1s spectrum consists of two peaks at 532.6 and 533.8 eV, which are characteristic for carboxyl and alcohol groups (Fig. S10) [45,46]. The spectrum of the PECVD BCN film is significantly different from the discussed above. The photoelectron peak of B 1s has a dominant component at 190.7 eV, which corresponds to h-BN compound (the boron atom is coordinated by three nitrogen atoms -BN_3). Additionally, low intensity components at 189.6, 190.3 and 191.9 eV, which can be interpreted as B–C bonds and the hybrid B-(C_nN_{3-n}) and B-$(C/N)_nO_{3-n}$ bonds, respectively. C 1s spectral region exhibits a complex profile, resulting from the overlap of four distinct components. The dominant peak appears at a binding energy of 284.8 eV, which is attributed to sp^2 C as well as to carbon-containing surface impurities. The peaks at 282.9,

286.6 and 288.5 eV correspond to C–B, C-(B_nN_{3-n}) and C-B_nN_{3-n} hybrid bonds. N 1s spectrum has one intense peak at 398.2 eV, which corresponds to h-BN, and two low intensity components at 399.0 and 400.0 eV, corresponding to N-(B_nC_{3-n}) and N-$(B/C)_nO_{3-n}$ hybrid bonds. O 1s spectrum is mainly located at 532.4 and 533.7 eV, which correspond to the chemical bonds in the carboxyl and the alcohol group respectively. These findings confirm that the one-stop approach enables growth of a bilayer structure with precise control of the BC_x and BCN composition. Furthermore, the XPS results are consistent with the EDX, FTIR and Raman spectroscopy data, providing a comprehensive understanding of the film's chemical characteristics.

3.2. PEC performance evaluation

The photoelectrochemical (PEC) water oxidation performance of BCN photoanodes modified with a BC_x tuning layer was evaluated in 1 M KOH solution under AM 1.5G simulated solar radiation (100 mW cm^{-2}). To elucidate the role of BC_x tuning layer in promoting electron transport, the PEC activities of BC_x, BCN and BCN/BC_x grown on FTO were compared. As shown in Fig. 3a, the BC_x photoanode displayed a weak photocurrent response (0.05 mA cm^{-2} at 1.23 V), likely due to a large overpotential for oxygen evolution reaction caused by the lack of a surface catalyst to drive the reaction efficiently [29,47]. Furthermore, the evaluation of the BC_x conductivity revealed that the BC_x layer exhibits outstanding electron transport efficiency, making it suitable as an electron transport layer (Table S2). Remarkably, the BCN photoanode modified with a BC_x electron transport layer exhibited a significantly enhanced photocurrent density of 0.82 mA cm^{-2} at 1.23 V, which is 4.6 times higher than pristine BCN (0.18 mA cm^{-2}). Meanwhile, the effect of BC_x functional layer thickness on photoanode performance was investigated. The highest PEC activity was achieved when the BC_x layer exhibited a moderate thickness (Figs. S11–S12). As shown in Fig. S13, the slope of the BCN/BC_x photoanode under illumination shows that the C_{dl} ratio is 17.7 % higher than that under dark conditions. The absorbed photon-to-current efficiency (ABPE) was calculated from the photocurrent density curves (Fig. 3b). The ABPE of the BCN/BC_x photoanode reached 0.02 % at 1.16 V, significantly higher than that of pristine BCN (0.005 % at 1.15 V) and BC_x (0.0025 % at 1.15 V). This enhancement is attributed to the vertically aligned nanostructured arrays and BC_x electron transport layers, which facilitate efficient light-harvesting and charge conversion (Fig. S7). To further investigate the electron recombination dynamics of the photoanodes, the decay of the open-circuit voltage over time under AM 1.5 G irradiation was examined (Fig. S14). The BCN/BC_x photoanode demonstrates a longer average carrier lifetime than the other samples, suggesting a slower voltage decay rate and more efficient separation of photogenerated electrons and holes.

To better focus on charge transport and separation inside the photoanode, the photocurrent of the BCN/BC_x, BCN and BC_x, was measured in a 0.5 M Na_2SO_3 solution as sacrificial reagent, where the limitations of surface OER dynamics can be ignored. The BCN displays an increased to photocurrent of 0.35 mA cm^{-2} at 1.23 V, which was further enhanced to

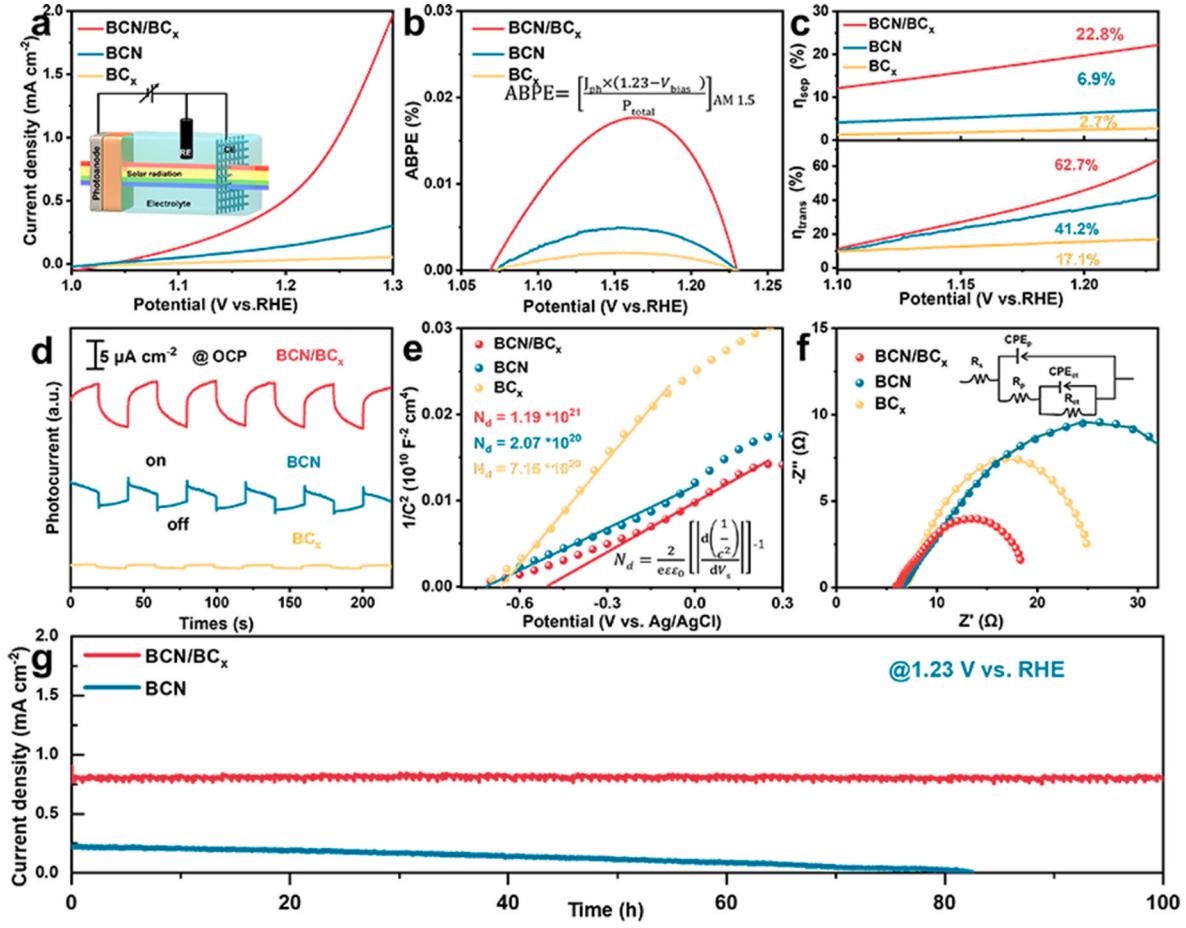

Fig. 3. (a) Linear-sweep voltammograms (LSV) measured in a 1 M KOH solution under AM 1.5G illumination (100 mW cm^{-2}) with a scan rate of 5 mV s^{-1}. (b) ABPE curves. (c) The calculated η_{sep} and η_{trans} curves. (d) Chopped illumination transient photocurrent response of different catalysts (BCN/BC_x, BCN and BC_x) at the open circuit potential within 0.5 M Na_2SO_4 solution. (e) Mott-Schottky plots for BCN/BC_x, BCN and BC_x samples collected at a frequency of 1 kHz in the dark. (f) Electrochemical impedance spectra (EIS) for the samples of BCN/BC_x, BCN and BC_x measured at 1.6 V under illumination. (g) The durability of the photoanode measured at 1.23 V.

1.2 mA cm^{-2} for the optimal BCN/BC_x (Fig. S15), implying that the introduction of the BC_x electron transport layer can facilitate charge separation and increase the photocurrent. The charge separation efficiency (η_{sep}) and charge transfer efficiency (η_{trans}) are estimated and shown in Fig. 3c. BCN/BC_x at 1.23 V versus RHE shows a η_{sep} of 22.8 %, 3.3 times higher than that BCN (6.9 %), indicating that charge recombination inside the photoanode was effectively retarded. Similarly, the introduction of BC_x electron transport layers enabled the BCN/BC_x photoanode to exhibit a higher η_{trans} at 1.23 V (increasing from 41.2 % to 62.7 %), indicating that the upward band alignment induced by the BC_x layer facilitates charge transfer in both the surface and bulk regions of the photoanode. Additionally, chronoamperometric *I-t* curves under chopped illumination were used to characterize the photoresponse of BC_x, BCN, and BCN/BC_x photoanodes. All photoanodes displayed rapid responses to incident light during on-off cycles (Fig. 3d and S16). Under open circuit potential (OCP) conditions, BCN/BC_x structure achieved a photocurrent density of 10 μA cm^{-2}, surpassing samples with both pristine BCN and BC_x. Notably, the *I-t* curves of BCN exhibited spike peaks, which are attributed to the rapid recombination of photogenerated electron-hole pairs upon light excitation. The incorporation of a BC_x tuning layer significantly suppresses this recombination process. This suppression highlights the role of BC_x in effectively reducing the recombination of photogenerated electron-hole pairs in BCN, thereby enhancing the PEC performance of the BCN photoanode.

To investigate the underlying cause of PEC enhancement, charge transfer kinetics were analyzed. Mott-Schottky (M-S) measurements (Fig. 3e and S17) of BC_x, BCN, and BCN/BC_x photoanodes were conducted at 1 kHz. The carrier concentration (N_d) is inversely proportional to the slope of the M-S plot [48]. Since the ultrathin film of BC_x minimally affects the basic composition of the BCN/BC_x materials, an equivalent dielectric constant was assumed for these devices [49,50]. The positive slopes in the M-S curves of all photoanodes confirm their n-type semiconductor characteristics. Beneficially, the slope of the BCN/BC_x photoanode was significantly smaller than those of BC_x and BCN, reflecting a higher carrier density is conducive to improving the charge transport. The calculated N_d values followed the trend: BCN (2.07×10^{20} cm^{-3}) < BC_x (7.16×10^{20} cm^{-3}) < BCN/BC_x (1.19×10^{21} cm^{-3}). This demonstrates that BC_x, acting as a tuning layer, significantly enhances the electronic conductivity of the photoanode. Additionally, BCN/BC_x and BC_x exhibited a positive shift in flat-band potential compared to BCN, indicating improved charge transport efficiency.

Electrochemical impedance spectroscopy (EIS) was employed to elucidate interfacial charge transfer and oxygen evolution kinetics. Nyquist plots in Fig. 3f reveal two characteristic arcs, attributed to bulk resistance (R_p) at high frequencies and interfacial charge-transfer resistance (R_{ct}) at low frequencies across the photoanode/electrolyte boundary [47]. EIS measurements (Fig. 3e) under AM 1.5 G simulated solar radiation revealed R_{ct} values of 38, 26, and 13 Ω for BCN, BC_x, and BCN/BC_x photoanodes, respectively. The significant reduction in Rct for the BCN/BC_x photoanode indicates that BC_x facilitates the transport of photoexcited carriers at the interface, effectively suppressing charge recombination and enhancing interfacial charge transfer kinetics [51]. Interestingly, the BCN/BC_x-X photoanodes exhibited a higher R_{ct} in the dark than under illumination. When the BC_x electron transport layer has moderate thickness, the difference R_{ct} between the dark and light conditions is the greatest. These results indicate that an appropriately engineered BC_x electron transport layer facilitates efficient interfacial charge transfer under illumination (Fig. S18).

As shown in Fig. S19, the vertically aligned nanowall array structure of the BCN/BC_x heterostructure remained intact with no phase change observed after the long-term stability test. The exceptional stability of the BCN/BC_x system is attributed to the BC_x tuning layer, which provides electron transfer energy levels that are well-matched. This energy band matching minimizes the recombination losses typically observed in BCN, further underscoring the superior performance of the BCN/BC_x system in photoelectrochemical applications [52]. Therefore, unmodified BCN exhibits lower photocurrent density and stability. However, after the introduction of the electron transport layer, the reduction of the interfacial reaction barrier accelerates charge transfer between the semiconductor and the active species in the electrolyte. This not only prevents the material from corrosion caused by charge accumulation but also enhances both the photocurrent density and stability of electrode [53]. The BC_x tuning layer strategy demonstrates broad applicability, as preliminarily validated by its extension to photo-assisted Zn-air batteries and Fe_2O_3-based photoanodes (Fig. S20), where it significantly enhances charge separation and overall device performance.

3.3. The water oxidation mechanism of photoanode

Further investigation using three-dimensional fluorescence revealed the fluorescence characteristics of BCN before and after the introduction of the tuning layer BC_x. Compared to pristine BCN, the use of the additional BC_x layer resulted in a blue shift in both excitation and emission wavelengths, indicating that the addition of BC_x layer altered the electronic structure of BCN and modified BCN/BC_x's band structure (Fig. 4a–c). This modification enhanced the light absorption efficiency, leading to a higher generation of photogenerated charge carriers, which is highly beneficial for PEC applications. Meanwhile, the optical properties of the nanofilm samples were examined by using photoluminescence (PL) and UV–Vis diffuse reflectance spectroscopy emission spectra. To evaluate charge separation capability, PL spectroscopy was conducted for the photoanodes using an excitation wavelength of 355 nm. As shown in Fig. 4d, BC_x displays a pronounced PL emission peak at 418 nm, linked to bandgap transitions and charge transfer transitions involving boron-rich sites. Compared to BC_x, the intensity of this emission peak is significantly reduced for BCN and is further diminished in the BCN/BC_x system. The reduction in PL emission intensity demonstrates the radiative recombination of photogenerated charge carriers is significantly suppressed, favoring electron-hole separation [60]. Moreover, time-resolved transient PL decay spectra recorded at the steady-state emission peaks revealed that the BCN/BC_x heterostructure exhibits a longer average carrier lifetime (τ_{avg}) than pristine BCN (Fig. 4e), indicating more efficient charge transfer in BCN/BC_x. UV–Vis absorption spectra (Fig. S21) revealed the optical characteristics of BC_x, BCN and BCN/BC_x photoanodes. Compared to pristine BCN, the introduction of the BC_x electron transport layer in the BCN/BC_x sample significantly enhances light absorption intensity, suggesting a positive impact on the remarkable improvement in PEC activity. Based on the transformed Lambert's function [61,62]. the intrinsic bandgaps of BC_x, BCN and BCN/BC_x were calculated to be 2.1, 3.9 and 3.2 eV, respectively (Fig. 4f). The increased absorbance in the visible light region upon introducing the BC_x layer is attributed to the visible light absorption properties of BCN and BC_x.

Based on these results, a possible mechanism for the significant enhancement of PEC behavior in the BCN/BC_x photoanode is proposed. According to the Mott-Schottky plots, the intercept on the horizontal axis corresponds to the flat-band potential [63]. Additionally, for n-type semiconductors, the flat-band potential is approximately 0.1 eV above the conduction band edge [64]. Consequently, the potential at the bottom of the conduction band (E_{CB}) can be derived, and valence band potential (E_{VB}) was then calculated using relationship $E_g = |E_{CB} - E_{VB}|$. Resulting band structures are illustrated in Fig. 4g and h. Because the conduction band of the BCN/BC_x catalyst has a higher reduction potential than that of pristine BCN, photoexcited electrons transfer from BCN to the conduction band of BC_x. This transfer prolongs the lifetime of localized electrons, suppresses charge recombination, and enhances charge separation, thereby making holes the primary active sites for the PEC reaction. Consequently, electron-hole recombination in BCN is inhibited, and the valence-band holes exhibit improved activity toward the oxidation of OH^- to O_2, which benefits PEC performance. In contrast, in BCN without a tuning layer, the transport of photogenerated

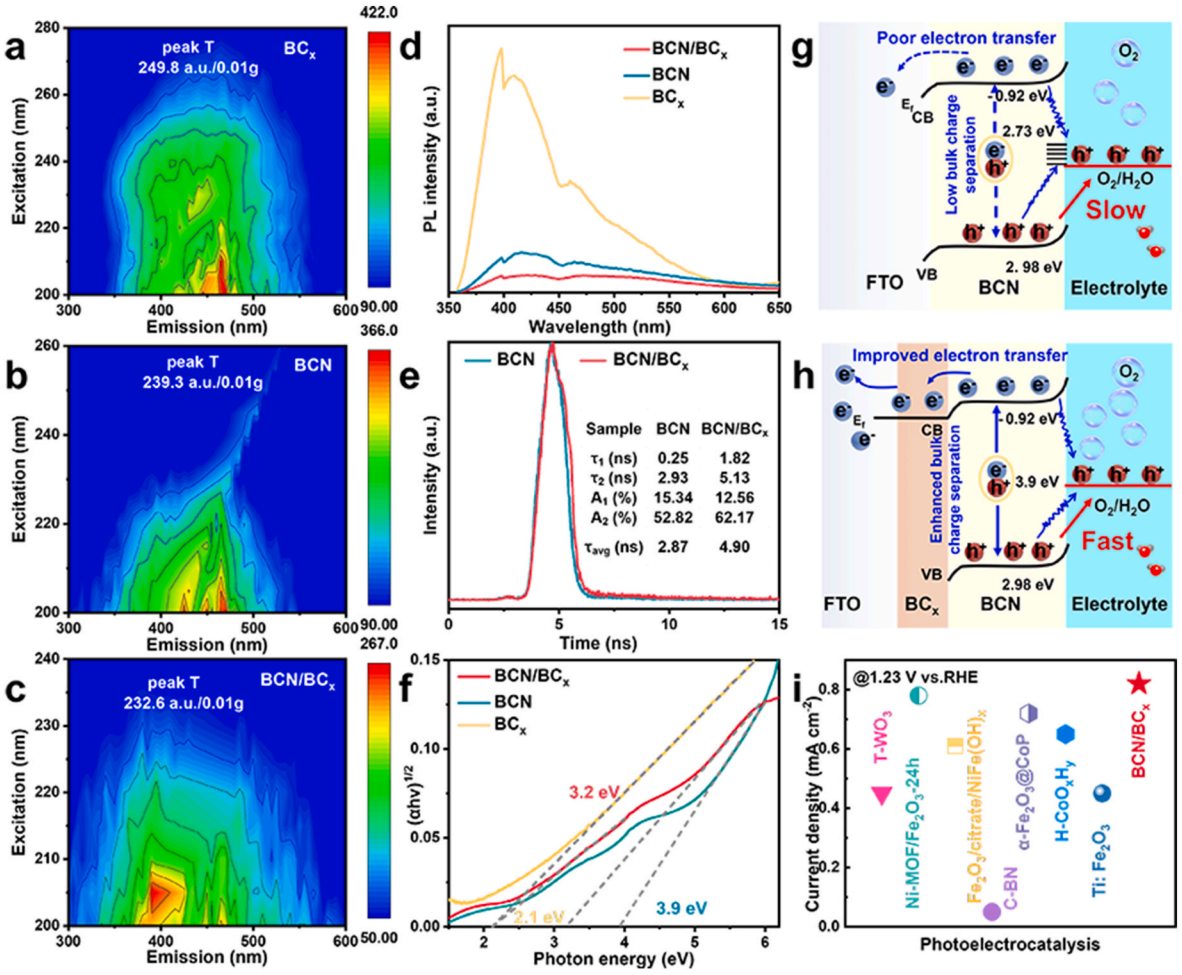

Fig. 4. (a–c) The 3D fluorescence spectra of BC_x, BCN and BCN/BC_x samples, respectively. (d) Steady-state Photoluminescence spectra, (e) and time-resolved transient PL decay spectra. (f) Tauc plots of BCN/BC_x, BCN and BC_x samples. (g, h) Charge transfer in the BCN photoanode with and without electronic transport layer with energy band diagram. (i) Comparison of BCN/BC_x sample and other PEC water oxidation performance [17,54–59].

electrons is severely hindered by the high interfacial energy barrier. Moreover, the holes generated by the photoanode upon excitation are largely blocked from reaching the surface active sites, with most holes recombining with photogenerated electrons rather than participating in the water oxidation reaction (Fig. 4g). In contrast, due to the strong electron transfer resulting from the interfacial bonding between the BCN photoanode and the BC_x catalyst (Fig. 4h), photogenerated holes can rapidly migrate from the photoanode to the catalyst surface, while the accumulated photogenerated electrons on BCN are quickly transferred through the electron transport layer to the electrode, significantly promoting charge separation and transfer. As summarized in Table S3 and Fig. S22, the photocurrent and stability runtime of the BCN/BC_x photoelectrochemical are compared with those of reported non-noble metal-based OER photocatalysts in alkaline media (Fig. 4i). The outstanding water oxidation activity of photoelectrocatalysis indicates significant potential for practical application in water splitting cells.

4. Conclusions

In summary, we have achieved synergistic control of BC_x tuning layer formation and vertical growth of boron carbonitride (BCN) nanostructures on FTO has been achieved through an integrated CVD synthesis approach. This functional layer of BC_x simultaneously suppresses charge recombination pathways in BCN nanowall arrays while enhancing light-trapping efficiency via the optimized photon scattering and multi-reflection phenomena within the vertically aligned nanoarchitecture. Furthermore, owing to its low conduction band, the BC_x layer facilitates the charge separation and transfer, significantly boosting the utilization efficiency of photogenerated electron-hole pairs in BCN photocatalysts. Mechanistic studies indicate that during photoelectrochemical reactions, electrons are effectively separated and transferred to the BC_x layer, while holes serve as the primary active species. With a higher carrier concentration (1.19×10^{21} cm^{-3}), the BCN/BC_x photoanode exhibits an increased photocurrent density, increasing from 0.18 to 0.82 mA cm^{-2}, along with excellent stability over 100 h. This work not only addresses the critical issue of severe electron-hole pair recombination in conventional semiconductor photoelectrodes but also underscores the pivotal role of the innovative tuning layer strategy in designing and synthesizing high-performance PEC devices.

CRediT authorship contribution statement

Lin Wu: Writing – review & editing, Writing – original draft, Visualization, Formal analysis, Conceptualization. **Svetlana V. Belaya:** Writing – review & editing, Supervision, Resources, Formal analysis. **Lixiang Li:** Validation, Supervision, Software, Resources. **Eugene A. Maksimovskiy:** Funding acquisition, Formal analysis, Data curation. **Alexei N. Kolodin:** Visualization, Methodology, Formal analysis, Data curation. **Igor P. Asanov:** Investigation, Formal analysis, Data curation, Conceptualization. **Alexandr G. Plekhanov:** Visualization, Validation, Resources, Methodology, Formal analysis. **Ilya V. Korolkov:**

Investigation, Formal analysis, Data curation. **Han Zhang:** Writing – review & editing, Validation, Supervision, Formal analysis. **Marina L. Kosinova:** Writing – review & editing, Supervision, Software, Resources, Investigation. **Baigang An:** Writing – review & editing, Resources, Project administration, Methodology, Investigation, Funding acquisition, Conceptualization.

Declaration of competing interest

The authors declare that they have no known competing financial interests or personal relationships that could have appeared to influence the work reported in this paper.

Acknowledgements

Financial supports by the National Natural Science Foundation of China No. 51872131, 52371224, 22109061. The Ministry of Science and Higher Education of the Russian Federation, No. 125021001790-0, 1250211302133 and No. 125021302132-4. The Fundamental Research Funds for the Liaoning Universities, No. LJ222410146062, and Liaoning University of Science and Technology Graduate Innovation and Entrepreneurship Project (No. LKDYC202303) are acknowledged.

Appendix A. Supplementary data

Supplementary data to this article can be found online at https://doi.org/10.1016/j.carbon.2025.120926.

References

[1] A. Mei, X. Li, L. Liu, Z. Ku, T. Liu, Y. Rong, M. Xu, M. Hu, J. Chen, Y. Yang, A hole-conductor–free, fully printable mesoscopic perovskite solar cell with high stability, Science 345 (6194) (2014) 295–298.
[2] S. Mathew, A. Yella, P. Gao, R. Humphry-Baker, B.F. Curchod, N. Ashari-Astani, I. Tavernelli, U. Rothlisberger, M.K. Nazeeruddin, M. Grätzel, Dye-sensitized solar cells with 13% efficiency achieved through the molecular engineering of porphyrin sensitizers, Nat. Chem. 6 (3) (2014) 242–247.
[3] D. Bao, Q. Zhang, F.L. Meng, H.X. Zhong, M.M. Shi, Y. Zhang, J.M. Yan, Q. Jiang, X. B. Zhang, Electrochemical reduction of N_2 under ambient conditions for artificial N_2 fixation and renewable energy storage using N_2/NH_3 cycle, Adv. Mater. 29 (3) (2017) 1604799.
[4] H.-H. Li, Q.-Q. Fu, L. Xu, S.-Y. Ma, Y.-R. Zheng, X.-J. Liu, S.-H. Yu, Highly crystalline PtCu nanotubes with three dimensional molecular accessible and restructured surface for efficient catalysis, Energy Environ. Sci. 10 (8) (2017) 1751–1756.
[5] E. Verlage, S. Hu, R. Liu, R.J. Jones, K. Sun, C. Xiang, N.S. Lewis, H.A. Atwater, A monolithically integrated, intrinsically safe, 10% efficient, solar-driven water-splitting system based on active, stable earth-abundant electrocatalysts in conjunction with tandem III–V light absorbers protected by amorphous TiO_2 films, Energy Environ. Sci. 8 (11) (2015) 3166–3172.
[6] W.-J. Ong, L.-L. Tan, Y.H. Ng, S.-T. Yong, S.-P. Chai, Graphitic carbon nitride (g-C_3N_4)-based photocatalysts for artificial photosynthesis and environmental remediation: are we a step closer to achieving sustainability? Chem. Rev. 116 (12) (2016) 7159–7329.
[7] G. Liao, Y. Gong, L. Zhang, H. Gao, G.-J. Yang, B. Fang, Semiconductor polymeric graphitic carbon nitride photocatalysts: the "holy grail" for the photocatalytic hydrogen evolution reaction under visible light, Energy Environ. Sci. 12 (7) (2019) 2080–2147.
[8] B. Tian, Y. Wu, G. Lu, Metal-free plasmonic boron phosphide/graphitic carbon nitride with core-shell structure photocatalysts for overall water splitting, Appl. Catal. B Environ. 280 (2021) 119410.
[9] M. Zhou, S. Wang, P. Yang, C. Huang, X.J. Wang, Boron carbon nitride semiconductors decorated with CdS nanoparticles for photocatalytic reduction of CO_2, ACS Catal. 8 (6) (2018) 4928–4936.
[10] J. Liu, S. Wen, Y. Hou, F. Zuo, G.J. Beran, P. Feng, Boron carbides as efficient, metal-free, visible-light-responsive photocatalysts, Angew. Chem. Int. Ed. 52 (11) (2013) 3241–3245.
[11] Y. Kong, X. Li, A.R. Puente Santiago, T. He, Nonmetal atom doping induced orbital shifts and charge modulation at the edge of two-dimensional boron carbonitride leading to enhanced photocatalytic nitrogen reduction, J. Am. Chem. Soc. 146 (9) (2024) 5987–5997.
[12] S.A. Thomas, J. Cherusseri, Boron carbon nitride (BCN): an emerging two-dimensional nanomaterial for supercapacitors, J. Mater. Chem. A 11 (43) (2023) 23148–23187.
[13] H. Sohrabi, O. Arbabzadeh, M. Falaki, V. Vatanpour, M.R. Majidi, N. Kudaibergenov, S.W. Joo, A. Khataee, Advances in fabrication, physio-chemical properties, and sensing applications of non-metal boron nitride and boron carbon nitride-based nanomaterials, Surf. Interfaces 41 (2023) 103152.
[14] M. Kaur, K. Singh, A. Vij, A. Kumar, Recent insights into BCN nanomaterials–synthesis, properties and applications, New J. Chem. 47 (5) (2023) 2137–2160.
[15] H.-W. Zhang, Y.-Y. Li, W.-Q. Huang, B.-X. Zhou, S.-F. Ma, Y.-X. Lu, A.-L. Pan, G.-F. Huang, Hollow BCN microrods with hierarchical multichannel structure as a multifunctional material: synergistic effects of structural topology and composition, Carbon 148 (2019) 231–240.
[16] M.M. Hasan, G.E. Khedr, F. Zakaria, N.K. Allam, Intermolecular electron transfer in electrochemically exfoliated BCN-Cu nanosheet electrocatalysts for efficient hydrogen evolution, ACS Appl. Energy Mater. 5 (8) (2022) 9692–9701.
[17] Y. Fang, I.S. Merenkov, X. Li, J. Xu, S. Lin, M.L. Kosinova, X. Wang, Vertically aligned 2D carbon doped boron nitride nanofilms for photoelectrochemical water oxidation, J. Mater. Chem. A 8 (26) (2020) 13059–13064.
[18] Y. Gong, X. Quan, H. Yu, S. Chen, H. Zhao, Enhanced photocatalytic performance of a two-dimensional $BiOIO_3$/g-C_3N_4 heterostructured composite with a Z-scheme configuration, Appl. Catal. B Environ. 237 (2018) 947–956.
[19] L. Acharya, S. Nayak, S.P. Pattnaik, R. Acharya, K.J. Parida, Resurrection of boron nitride in pn type-II boron nitride/B-doped-g-C_3N_4 nanocomposite during solid-state Z-scheme charge transfer path for the degradation of tetracycline hydrochloride, J. Colloid Interface Sci. 566 (2020) 211–223.
[20] H. Zhong, C. Yang, L. Fan, Z. Fu, X. Yang, X. Wang, R. Wang, Dyadic promotion of photocatalytic aerobic oxidation via the Mott-Schottky effect enabled by nitrogen-doped carbon from imidazolium-based ionic polymers, Energy Environ. Sci. 12 (1) (2019) 418–426.
[21] F. Xing, Q. Liu, M. Song, C. Huang, Fluorine modified boron carbon nitride semiconductors for improved photocatalytic CO_2 reduction under visible light, ChemCatChem 10 (22) (2018) 5270–5279.
[22] M.A. Ahsan, T. He, K. Eid, A.M. Abdullah, M.L. Curry, A. Du, A.R. Puente Santiago, L. Echegoyen, J.C. Noveron, Tuning the intermolecular electron transfer of low-dimensional and metal-free BCN/C_{60} electrocatalysts via interfacial defects for efficient hydrogen and oxygen electrochemistry, J. Am. Chem. Soc. 143 (2) (2021) 1203–1215.
[23] E. Hou, S. Cheng, Y. Qiu, X. Chen, J. Chen, C. Sun, H. Zhang, J. Yang, X. Zhao, L. Xie, Cross-linkable fullerene electron transport layer with internal encapsulation capability for efficient and stable inverted perovskite solar cells, Angew. Chem. 137 (4) (2025) e202416703.
[24] C. Liang, Z.-A. Lu, M. Zheng, M. Chen, Y. Zhang, B. Zhang, J. Zhang, P. Xu, Band structure engineering within two-dimensional borocarbonitride nanosheets for surface-enhanced Raman scattering, Nano Lett. 22 (16) (2022) 6590–6598.
[25] D. Shi, B. Chang, Z. Ai, H. Jiang, F. Chen, Y. Shao, J. Shen, Y. Wu, X.J.N. Hao, Boron carbonitride with tunable B/N Lewis acid/base sites for enhanced electrocatalytic overall water splitting, Nanoscale 13 (5) (2021) 2849–2854.
[26] T. Yuan, M. Zheng, M. Antonietti, X. Wang, Ceramic boron carbonitrides for unlocking organic halides with visible light, Chem. Sci. 12 (18) (2021) 6323–6332.
[27] K.K. Kim, H.S. Lee, Y.H. Lee, Synthesis of hexagonal boron nitride heterostructures for 2D van der Waals electronics, Chem. Soc. Rev. 47 (16) (2018) 6342–6369.
[28] Y. Uchida, S. Nakandakari, K. Kawahara, S. Yamasaki, M. Mitsuhara, H. Ago, Controlled growth of large-area uniform multilayer hexagonal boron nitride as an effective 2D substrate, ACS Nano 12 (6) (2018) 6236–6244.
[29] Y. Liu, Z. Zhang, K. Wang, X. Tan, J. Chen, X. Ren, F. Jiang, Efficient $BiVO_4$ photoanode with an excellent hole transport layer of CuSCN for solar water oxidation, Adv. Energy Mater. 14 (17) (2024) 2304223.
[30] S.V. Belaya, E.A. Maksimovsky, V.R. Shayapov, A.A. Shapovalova, A.N. Kolodin, A. A. Saraev, I.P. Asanov, M.N. Khomyakov, I.V. Yushina, A.G. Plekhanov, Boron carbonitride films with tunable composition: LPCVD and PECVD synthesis using trimethylamine borane and nitrogen mixture and characterization, Appl. Sci. 13 (8) (2023) 4959.
[31] T. Yuan, L. Sun, Z. Wu, R. Wang, X. Cai, W. Lin, M. Zheng, X. Wang, Mild and metal-free Birch-type hydrogenation of (hetero) arenes with boron carbonitride in water, Nat. Catal. 5 (12) (2022) 1157–1168.
[32] L. Cao, T. Yang, H. Mo, Y. Zhang, Y. Gao, Z. Xu, B. Kang, X. Xia, W. Zhang, Z. Xu, (B, N)-Rich B-C-N nanosheet-assembled microwires as effective electrocatalysts for oxygen reduction reaction, Chem. Nano Mater. 10 (3) (2024) e202300487.
[33] L. Qin, J. Yu, S. Kuang, C. Xiao, X. Bai, Few-atomic-layered boron carbonitride nanosheets prepared by chemical vapor deposition, Nanoscale 4 (1) (2012) 120–123.
[34] F.-J. Haug, C. Ballif, Light management in thin film silicon solar cells, Energy Environ. Sci. 8 (3) (2015) 824–837.
[35] R. Geick, C. Perry, G. Rupprecht, Normal modes in hexagonal boron nitride, Phys. Rev. 146 (2) (1966) 543.
[36] V.P. Tolstoy, I. Chernyshova, V.A. Skryshevsky, Handbook of Infrared Spectroscopy of Ultrathin Films, John Wiley & Sons2003.
[37] A. Rozenberg, Y.A. Sinenko, N. Chukanov, Ir spectroscopy characterization of various types of structural irregularities in pyrolytic boron nitride, J. Mater. Sci. 28 (1993) 5675–5678.
[38] F. Tuinstra, J.L. Koenig, Raman spectrum of graphite, J. Chem. Phys. 53 (3) (1970) 1126–1130.
[39] I. Merenkov, I. Kasatkin, E. Maksimovskii, N. Alferova, M. Kosinova, Vertically aligned layers of hexagonal boron nitride: PECVD synthesis from triethylaminoborane and structural features, J. Struct. Chem. 58 (2017) 1018–1024.
[40] J. Zhong, J. Huang, Y. Liu, D. Li, C. Tan, P. Chen, H. Liu, X. Zheng, C. Wen, W. Lv, Construction of double-functionalized g-C_3N_4 heterojunction structure via optimized charge transfer for the synergistically enhanced photocatalytic

degradation of sulfonamides and H_2O_2 production, J. Hazard Mater. 422 (2022) 126868.
[41] S. Nehate, A. Saikumar, A. Prakash, K. Sundaram, A review of boron carbon nitride thin films and progress in nanomaterials, Mater. Today Adv. 8 (2020) 100106.
[42] C. Wang, J. Xiao, Q. Shen, L. Zhang, Bonding structure and mechanical properties of BCN thin films synthesized by pulsed laser deposition at different laser fluences, Thin Solid Films 603 (2016) 323–327.
[43] G. Puyoo, F. Teyssandier, R. Pailler, C. Labrugère, G. Chollon, Boron carbonitride coatings synthesized by LPCVD, structure and properties, Carbon 122 (2017) 19–46.
[44] A. Prakash, K.B. Sundaram, Optical and XPS studies of BCN thin films by co-sputtering of B_4C and BN targets, Appl. Surf. Sci. 396 (2017) 484–491.
[45] H. Werheit, M.H. Manghnani, U. Kuhlmann, A. Hushur, S. Shalamberidze, Mode Grüneisen parameters of boron carbide, Solid State Sci. 72 (2017) 80–93.
[46] C. Ramana, R. Vemuri, V. Kaichev, V. Kochubey, A. Saraev, V. Atuchin, Interfaces, X-ray photoelectron spectroscopy depth profiling of La_2O_3/Si thin films deposited by reactive magnetron sputtering, ACS Appl. Mater. 3 (11) (2011) 4370–4373.
[47] R. Chong, Z. Wang, J. Lv, J. Rong, L. Zhang, Y. Jia, L. Wang, Z. Chang, X. Wang, A hybrid CoOOH-rGO/Fe_2O_3 photoanode with spatial charge separation and charge transfer for efficient photoelectrochemical water oxidation, J. Catal. 399 (2021) 170–181.
[48] K. Wang, D. Huang, L. Li, K. Feng, T. Harada, S. Ikeda, J. Li, F. Jiang, Three-dimensional GeSe microstructured air brick photocathode for advanced solar water splitting, Sol. RRL 4 (5) (2020) 1900559.
[49] P.I. Dankov, Concept for equivalent dielectric constant of planar transmission lines on anisotropic substrates. 2016 46th European Microwave Conference (EuMC), 2016, pp. 158–161.
[50] S.A. Gregory, R. Hanus, A. Atassi, J.M. Rinehart, J.P. Wooding, A.K. Menon, M. D. Losego, G.J. Snyder, S.K. Yee, Quantifying charge carrier localization in chemically doped semiconducting polymers, Nat. Mater. 20 (10) (2021) 1414–1421.
[51] Q. Zhi, W. Liu, R. Jiang, X. Zhan, Y. Jin, X. Chen, X. Yang, K. Wang, W. Cao, D. Qi, Piperazine-linked metalphthalocyanine frameworks for highly efficient visible-light-driven H_2O_2 photosynthesis, J. Am. Chem. Soc. 144 (46) (2022) 21328–21336.
[52] J. Luo, S. Zhang, M. Sun, L. Yang, S. Luo, J.C. Crittenden, A critical review on energy conversion and environmental remediation of photocatalysts with remodeling crystal lattice, surface, and interface, ACS Nano 13 (9) (2019) 9811–9840.
[53] W. Li, J. Shi, K.H. Zhang, J.L. MacManus-Driscoll, Defects in complex oxide thin films for electronics and energy applications: challenges and opportunities, Mater. Horiz. 7 (11) (2020) 2832–2859.
[54] J. Xie, P. Yang, X. Liang, J. Xiong, Self-improvement of ti: Fe_2O_3 photoanodes: photoelectrocatalysis improvement after long-term stability testing in alkaline electrolyte, ACS Appl. Energy Mater. 1 (6) (2018) 2769–2775.
[55] Y. Yi, Q. Wu, W. Wang, C. Cui, In situ depositing an ultrathin CoO_xH_y layer on hematite in alkaline media for photoelectrochemical water oxidation, Appl. Catal. B Environ. 263 (2020) 118334.
[56] T.-T. Li, Q. Zhou, J. Qian, Y. Hu, Y.-Q. Zheng, Electrodeposition of a cobalt phosphide film for the enhanced photoelectrochemical water oxidation with α-Fe_2O_3 photoanode, Electrochim. Acta 307 (2019) 92–99.
[57] J. Zhang, J. Cui, S. Eslava, Oxygen evolution catalysts at transition metal oxide photoanodes: their differing roles for solar water splitting, Adv. Energy Mater. 11 (13) (2021) 2003111.
[58] X. Liu, F. Zhan, D. Li, M. Xue, α-Fe_2O_3 nanoarrays photoanodes decorated with Ni-MOFs for enhancing photoelectrochemical water oxidation, Int. J. Hydrogen Energy 45 (53) (2020) 28836–28846.
[59] X. Shi, Q. Wu, C. Cui, Modulating WO_3 crystal orientation to suppress hydroxyl radicals for sustainable solar water oxidation, ACS Catal. 13 (2) (2023) 1470–1476.
[60] Y. Tan, Z. Shu, J. Zhou, T. Li, W. Wang, Z. Zhao, One-step synthesis of nanostructured g-C_3N_4/TiO_2 composite for highly enhanced visible-light photocatalytic H_2 evolution, Appl. Catal. B Environ. 230 (2018) 260–268.
[61] D. Zhao, J. Chen, C.-L. Dong, W. Zhou, Y.-C. Huang, S.S. Mao, L. Guo, S. Shen, Interlayer interaction in ultrathin nanosheets of graphitic carbon nitride for efficient photocatalytic hydrogen evolution, J. Catal. 352 (2017) 491–497.
[62] D. Zhao, C.L. Dong, B. Wang, C. Chen, Y.C. Huang, Z. Diao, S. Li, L. Guo, S. Shen, Synergy of dopants and defects in graphitic carbon nitride with exceptionally modulated band structures for efficient photocatalytic oxygen evolution, Adv. Mater. 31 (43) (2019) 1903545.
[63] K. Gelderman, L. Lee, S. Donne, Flat-band potential of a semiconductor: using the Mott–Schottky equation, J. Chem. Educ. 84 (4) (2007) 685.
[64] Z. Wei, M. Liu, Z. Zhang, W. Yao, H. Tan, Y. Zhu, Efficient visible-light-driven selective oxygen reduction to hydrogen peroxide by oxygen-enriched graphitic carbon nitride polymers, Energy Environ. Sci. 11 (9) (2018) 2581–2589.